Mon. Not. R. Astron. Soc. **000**, 1–9 (2016) Printed 21 April 2016 (MN LATEX style file v2.2)

Low-radio-frequency eclipses of the redback pulsar J2215+5135 observed in the image plane with LOFAR

J. W. Broderick,[1,2,3⋆] R. P. Fender,[1,2] R. P. Breton,[4,2] A. J. Stewart,[1,2] A. Rowlinson,[3,5] J. D. Swinbank,[6,5] J. W. T. Hessels,[3,5] T. D. Staley,[1,2] A. J. van der Horst,[7] M. E. Bell,[8,9] D. Carbone,[5] Y. Cendes,[5] S. Corbel,[10,11] J. Eislöffel,[12] H. Falcke,[13,3] J.-M. Grießmeier,[14,11] T. E. Hassall,[1,2] P. Jonker,[15,13] M. Kramer,[16,4] M. Kuniyoshi,[17] C. J. Law,[18] S. Markoff,[5] G. J. Molenaar,[5,19] M. Pietka,[1,2] L. H. A. Scheers,[20,5] M. Serylak,[21,22] B. W. Stappers,[4] S. ter Veen,[3] J. van Leeuwen,[3,5] R. A. M. J. Wijers,[5] R. Wijnands,[5] M. W. Wise[3,5] and P. Zarka[23,11]

[1]*Astrophysics, Department of Physics, University of Oxford, Keble Road, Oxford OX1 3RH, UK*
[2]*Physics and Astronomy, University of Southampton, Highfield, Southampton SO17 1BJ, UK*
[3]*ASTRON, the Netherlands Institute for Radio Astronomy, Postbus 2, 7990 AA Dwingeloo, The Netherlands*
[4]*Jodrell Bank Centre for Astrophysics, School of Physics and Astronomy, The University of Manchester, Manchester M13 9PL, UK*
[5]*Anton Pannekoek Institute for Astronomy, University of Amsterdam, Science Park 904, 1098 XH Amsterdam, The Netherlands*
[6]*Department of Astrophysical Sciences, Princeton University, Princeton, NJ 08544, USA*
[7]*Department of Physics, The George Washington University, 725 21st Street NW, Washington, DC 20052, USA*
[8]*CSIRO Astronomy and Space Science, PO Box 76, Epping, NSW 1710, Australia*
[9]*ARC Centre of Excellence for All-sky Astrophysics (CAASTRO), The University of Sydney, NSW 2006, Australia*
[10]*Laboratoire AIM (CEA/IRFU - CNRS/INSU - Université Paris Diderot), CEA DSM/IRFU/SAp, F-91191 Gif-sur-Yvette, France*
[11]*Station de Radioastronomie de Nançay, Observatoire de Paris, CNRS/INSU, USR 704 - Univ. Orléans, OSUC, 18330 Nançay, France*
[12]*Thüringer Landessternwarte, Sternwarte 5, D-07778 Tautenburg, Germany*
[13]*Department of Astrophysics/IMAPP, Radboud University Nijmegen, PO Box 9010, 6500 GL Nijmegen, The Netherlands*
[14]*LPC2E - Université d'Orléans / CNRS, 45071 Orléans cedex 2, France*
[15]*SRON, Netherlands Institute for Space Research, Sorbonnelaan 2, 3584 CA, Utrecht, The Netherlands*
[16]*Max-Planck-Institut für Radioastronomie, Auf dem Hügel 69, 53121 Bonn, Germany*
[17]*NAOJ Chile Observatory, National Astronomical Observatory of Japan, 2-21-1 Osawa, Mitaka, Tokyo 181-8588, Japan*
[18]*Department of Astronomy and Radio Astronomy Lab, University of California, Berkeley, CA, USA*
[19]*Department of Physics and Electronics, Rhodes University, PO Box 94, Grahamstown, 6140 South Africa*
[20]*Centrum Wiskunde & Informatica, Science Park 123, 1098 XG Amsterdam, The Netherlands*
[21]*Department of Physics & Astronomy, University of the Western Cape, Private Bag X17, Bellville 7535, South Africa*
[22]*SKA South Africa, 3rd Floor, The Park, Park Road, Pinelands, 7405, South Africa*
[23]*LESIA, Observatoire de Paris, CNRS, UPMC, Université Paris-Diderot, 5 place Jules Janssen, 92195 Meudon, France*

21 April 2016

ABSTRACT
The eclipses of certain types of binary millisecond pulsars (i.e. 'black widows' and 'redbacks') are often studied using high-time-resolution, 'beamformed' radio observations. However, they may also be detected in images generated from interferometric data. As part of a larger imaging project to characterize the variable and transient sky at radio frequencies < 200 MHz, we have blindly detected the redback system PSR J2215+5135 as a variable source of interest with the Low-Frequency Array (LOFAR). Using observations with cadences of 2 weeks – 6 months, we find preliminary evidence that the eclipse duration is frequency dependent ($\propto \nu^{-0.4}$), such that the pulsar is eclipsed for longer at lower frequencies, in broad agreement with beamformed studies of other similar sources. Furthermore, the detection of the eclipses in imaging data suggests an eclipsing medium that absorbs the pulsed emission, rather than scattering it. Our study is also a demonstration of the prospects of finding pulsars in wide-field imaging surveys with the current generation of low-frequency radio telescopes.

Key words: binaries: eclipsing; pulsars: general; pulsars: individual: PSR J2215+5135; radio continuum: stars

1 INTRODUCTION

The so-called 'black widow' and 'redback' pulsars have attracted considerable interest in recent years. First discovered by Fruchter, Stinebring & Taylor (1988), these binary systems consist of a millisecond pulsar and a low-mass companion star ($\lesssim 0.05$ $\mathrm{M}_{\odot}$ for black widows, and $\sim$0.1–0.4 $\mathrm{M}_{\odot}$ for redbacks); the companion, irradiated by the pulsar, is ablated (e.g. Kluzniak et al. 1988; van den Heuvel & van Paradijs 1988). Whether there is an evolutionary scenario linking the two classes remains unclear (e.g. Chen et al. 2013; Benvenuto, De Vito & Horvath 2014), although both are thought to be a link between accreting low-mass X-ray binary systems and 'recycled', rotation-powered millisecond pulsars (e.g. Archibald et al. 2009, 2015; Papitto et al. 2013; Patruno et al. 2014; Bassa et al. 2014; Stappers et al. 2014).

Deep radio pulsation searches towards unidentified *Fermi Gamma-Ray Space Telescope* sources (e.g. Ransom et al. 2011; Keith et al. 2011; Hessels et al. 2011; Ray et al. 2012; Bhattacharyya et al. 2013), as well as wide-field pulsar surveys and associated follow-up investigations (e.g. Stappers et al. 1996; Burgay et al. 2006; Crawford et al. 2013), have led to the total number of known black widows and redbacks in the Galactic field increasing to over twenty at present (review by Roberts 2013; also see Abdo et al. 2013 for the second *Fermi* pulsar catalogue). One of these new discoveries is the redback pulsar J2215+5135, identified by Hessels et al. (2011) in a 350-MHz survey with the Green Bank Telescope (GBT). It has a spin period of 2.61 ms, a dispersion measure (DM) of 69.2 pc cm^{-3}, and a 350-MHz flux density of $\sim$5 mJy. The orbital period, 4.14 h, is very similar to that of the prototypical Galactic field redback pulsar J1023+0038 (4.75 h; Archibald et al. 2009).

Breton et al. (2013) discovered the non-degenerate companion in the optical; from light curve modelling, it was found to have a minimum mass of $0.213\ \mathrm{M}_{\odot}$ and to be Roche lobe filling. In a similar study by Schroeder & Halpern (2014), two modelling routines yielded a companion mass of $0.345^{+0.008}_{-0.007}$ and $0.396 \pm 0.045\ \mathrm{M}_{\odot}$, respectively. Furthermore, the neutron star mass was constrained to be $> 1.75\ \mathrm{M}_{\odot}$, potentially making it one of the increasing number of known neutron stars with masses significantly in excess of the $1.4\ \mathrm{M}_{\odot}$ Chandrasekhar limit (Demorest et al. 2010; Romani et al. 2012; Antoniadis et al. 2013; Strader et al. 2015). However, a more recent study by Romani et al. (2015) suggests a lower neutron star mass of approximately $1.6\ \mathrm{M}_{\odot}$. Reported orbital inclination measurements range from approximately 50° to 90° (Breton et al. 2013; Schroeder & Halpern 2014; Romani et al. 2015).

Due to the presence of an intra-binary cloud or screen of material from the ablated companion, radio eclipses are observed in black widow and redback systems (e.g. Fruchter et al. 1988; Archibald et al. 2009). Although usually studied with high-time-resolution, 'beamformed'[1] observational modes, the sudden change in flux density due to eclipses can also be potentially detected in images generated from interferometric observations: if the imaging cadence is sufficiently well matched to the eclipse properties, then we would expect to see a variable compact source. In this paper, we report image-plane detections of the eclipses of PSR J2215+5135 with the Low-Frequency Array (LOFAR; van Haarlem et al. 2013). This source was at first blindly detected in the LOFAR 'Radio Sky Monitor' (RSM; we refer the reader to Fender et al. 2008, van Haarlem et al. 2013 and Swinbank et al. 2015); we then later used the full RSM data set and the known orbital ephemeris of the system to construct more complete light curves. We describe the LOFAR observations and data reduction in Section 2, and present our results in Section 3. In Section 4, we analyse the properties of the eclipses, before concluding in Section 5.

[1] We use the term 'beamformed' to describe pulsar-like observations.

Table 1. RSM beam centre coordinates for the observations used in this study. The observing strategy is described in Sections 2.1 and 2.2.

Observation	RA (J2000) (h m s)	Dec. (J2000) (° ′ ″)
HBA Pointing 1		
Beam 1	21 52 30.00	+50 56 27.7
Beam 2	21 52 30.00	+54 51 32.3
Beam 3	22 00 00.00	+52 54 00.0
Beam 4	22 07 30.00	+50 56 27.7
Beam 5	22 07 30.00	+54 51 32.3
Beam 6	22 15 00.00	+52 54 00.0
HBA Pointing 2		
Beam 1	22 22 30.00	+50 56 27.7
Beam 2	22 22 30.00	+54 51 32.3
Beam 3	22 30 00.00	+52 54 00.0
Beam 4	22 37 30.00	+50 56 27.7
Beam 5	22 37 30.00	+54 51 32.3
Beam 6	22 45 00.00	+52 54 00.0
LBA Beam 1	22 00 00.00	+52 54 00.0
LBA Beam 2	22 15 00.00	+48 58 55.4

2 LOFAR OBSERVATIONS

A detailed overview of LOFAR can be found in van Haarlem et al. (2013). Here, we provide a summary of our subset of observations from the LOFAR RSM, a project whose main goal is to characterize the low-frequency variable and transient radio sky over very large fields of view. We used both the high-band antennas (HBA; 110–240 MHz) and low-band antennas (LBA; 30–80 MHz).

2.1 HBA

Seven HBA observing runs were carried out over the period 2013 February – 2014 January (Tables 1 and 2). In each run, we obtained observations of two sets of six coordinates; these beams are part of a larger hexagonal mosaicking pattern designed to tile the entire zenith region for LOFAR (Dec. $\sim$+53°). The six beams for each pointing were observed simultaneously for 2×15 min, centred on transit. Each 15-min block comprised 2 min on the flux calibrator, Cygnus A, followed by 11 min on the RSM fields. The remaining 2×1 min was necessary to switch from the calibrator to the RSM fields, and vice versa. Thus, after 30 min, 22 min had been spent on-source; we then immediately observed the second set of six beams.

The 'HBA Dual Inner' array configuration was used for all observations, which results in a consistent primary beam size (and hence field of view) for the Dutch 'core' and 'remote' stations. The primary beam full width at half maximum (FWHM) at 150 MHz is 3.80°. There were a total of 36 or 37 Dutch stations available for each of the runs; no international stations were included. Projected baseline lengths ranged from about 43 m – 120 km.

All observations had a bandwidth of 46.9 MHz, covered by 240 sub-bands, each with an individual bandwidth of 195.3 kHz.

We placed 4×10 sub-bands (i.e. 4×1.95 MHz) on each of the six beams, with centre frequencies of 124, 149, 156 and 185 MHz.

2.2 LBA

Three LBA observing runs were conducted over the period 2013 August – 2014 March (Tables 1 and 3). We used two separate beams in this study, in which PSR J2215+5135 is either 2.6° or 2.7° from the phase centre. Each observation was 1 h in duration; the two RSM beams and the calibrator, Cygnus A (centred in a third separate beam), were observed simultaneously. The array configuration was 'LBA Inner', which maximizes the field of view (primary beam FWHM 9.77° at 60 MHz). As for the HBA observations, a total of 36 or 37 Dutch stations were available for each of the runs, with the projected baselines ranging from about 91 m – 84 km.

In addition, we have used the two bands where the bandpass response is most sensitive; the centre frequencies are 54 and 60 MHz. The bandwidth centred on each of these frequencies, per beam, was 3.3 MHz (17 sub-bands, each with individual bandwidth 195.3 kHz).

2.3 Data pre-processing

Pre-processing was carried out using standard methods. Firstly, radio-frequency interference (RFI) was removed using AOFLAGGER (Offringa et al. 2010; Offringa, van de Gronde & Roerdink 2012a; Offringa, de Bruyn & Zaroubi 2012b). Secondly, we used the 'demixing' algorithm (van der Tol, Jeffs & van der Veen 2007) to subtract the response due to very bright 'A-team' sources: Cassiopeia A in the high band, and both Cassiopeia A and Cygnus A in the low band (apart from Cygnus A in the calibrator scans).

Our observations were conducted during the early period of full LOFAR science operations, and, as such, optimal demixing settings had not yet been established. In the high band, the runs from 2013 March 24 – July 14 inclusive were processed slightly differently, which afterwards was found to have resulted in poorer-quality images. For the final HBA run on 2014 January 15, we reverted to the demixing settings used in the first two runs on 2013 February 10 and March 10.

For practical reasons concerning data volume and the computing time required for calibration and imaging, we also averaged the data in both time and frequency, typically to final resolutions of 10 s per time-step and 4 channels per sub-band. Bandwidth and time smearing effects (e.g. Bridle & Schwab 1999) are both negligible for this study.

2.4 Calibration and imaging

Calibration and imaging were also carried out using standard practices. The Cygnus A data were calibrated using a preliminary low-frequency LOFAR model of the source (McKean et al. 2011; McKean, priv. comm.). Phase-only calibration of the target fields used data from the global sky model developed by Scheers (2011). The 74 MHz Very Large Array (VLA) Low-Frequency Sky Survey (VLSS; Cohen et al. 2007) was the basis for these models; spectral indices[2] were obtained by cross-correlating the VLSS with the 325 MHz Westerbork Synthesis Radio Telescope (WSRT) Northern Sky Survey (WENSS; Rengelink et al. 1997) and the 1.4 GHz NRAO VLA Sky Survey (NVSS; Condon et al. 1998).

For each of the separate bands and beams, primary-beam-corrected images were made with the AWIMAGER (Tasse et al. 2013). We used a robust weighting parameter (Briggs 1995) of 0. For the HBA data, we restricted the projected baseline range to 0.1–6 kλ (200 m – 12 km at 150 MHz), and 0.04–1.2 kλ for the LBA observations (200 m – 6 km at 60 MHz). These baseline ranges were determined empirically to ensure reliable images, given both the limitations of the uv coverage per run, as well as our relatively rudimentary calibration procedure.

We concatenated the 2×11 min HBA snapshots prior to imaging; the resulting maps for the six beams were then mosaicked together to create the final set of images, i.e. separate 22-min mosaics at each of the four central frequencies, per pointing. In the low band, we divided the 60-min data sets into 3×20 min segments, and created separate maps for each frequency and beam. The median angular resolutions are approximately 60 arcsec $\times$ 30 arcsec (HBA), and 280 arcsec $\times$ 140 arcsec (LBA).

In the 2013 February 10, 2013 March 10 and 2014 January 15 HBA mosaics, the typical rms noise level near PSR J2215+5135 is about 10–15 mJy beam^{-1}. However, on average, it is a factor of $\sim$2–2.5 worse in the remaining HBA runs, where the demixing settings had been changed. In the LBA, the noise level ranges from about 190–660 mJy beam^{-1}. For both the HBA and LBA observations, the noise levels are above the nominal confusion limits by factors of $\sim$2–4 in the best-case scenarios. This is likely to be a consequence of both our simple calibration strategy and residual signal from Cassiopeia A, which is only 12° from PSR J2215+5135. Attempts at further phase-only self-calibration did not result in significant differences to either the image dynamic range or the source flux densities.

We estimate that the internal calibration uncertainty across all of the runs ranges from 15–20 per cent in the high band, depending on the demixing settings used. In the low band, it is about 30 per cent. The absolute flux scale is that of Baars et al. (1977).

3 RESULTS

We detected a variable source at the following coordinates: RA $22^{\rm h}15^{\rm m}32\overset{\rm s}{.}4$, Dec. $+51^\circ35'39''$ (J2000). We estimate that the position is accurate to within approximately 5 arcsec (in the high band); thus, the coordinates are in agreement with the position of PSR J2215+5135 derived from beamformed observations (Abdo et al. 2013; Hessels et al. in prep.).

Initially, the discovery was made from visual inspection of the HBA data from 2013 February 10 and March 10, as well as 2014 January 15 (Figure 1). The variability was subsequently confirmed with the TRANSIENTS PIPELINE (TRAP; Swinbank et al. 2015). Then, as mentioned in Section 1, we used the full RSM data set to obtain more complete source properties for PSR J2215+5135.

Measured flux densities from point-source Gaussian fits are presented in Tables 2 and 3. We used IMFIT in MIRIAD (Sault, Teuben & Wright 1995) for this task, and confirmed the results using PYSE (Spreeuw 2010). For the low signal-to-noise (S/N) detections, we report the fitted flux density from a forced point-source fit at the source location, rather than an upper limit, to allow for improved light curve modelling (Section 4.2). In a handful of the noisiest images, we instead estimated the flux density based on the integrated pixel sum in a box surrounding the source position.

[2] In this paper, we use the convention $S_\nu \propto \nu^\alpha$, where S_ν is the flux density at frequency ν, and α is the spectral index.

Table 2. LOFAR high-band image-plane observations of PSR J2215+5135. MJD is the Modified Julian Date at the halfway point of each observation (in Coordinated Universal Time; UTC), and ϕ is the orbital phase determined using the ephemeris of Abdo et al. (2013) and Hessels et al. (in prep.). Orbital phases are defined such that the superior conjunction of the pulsar is at $\phi = 0.5$. A description of how the flux densities were measured can be found in Section 3. Spectral indices across the high band were determined from linear least-squares fits in $\log(S_\nu)$–$\log(\nu)$ space, with inverse-variance weighting. All uncertainties are $\pm1\sigma$. We also give the LOFAR observation IDs for each epoch.

Date	MJD	ϕ (range)	$S_{124\,\mathrm{MHz}}$ (mJy)	$S_{149\,\mathrm{MHz}}$ (mJy)	$S_{156\,\mathrm{MHz}}$ (mJy)	$S_{185\,\mathrm{MHz}}$ (mJy)	α_{HBA}	IDs (range)
2013 February 10	56333.509	0.381–0.486	18 ± 15	-15 ± 9	1 ± 9	-4 ± 9		L89610–
	56333.530	0.502–0.606	3 ± 13	-1 ± 10	5 ± 10	8 ± 12		L89617
2013 March 10	56361.431	0.242–0.347	57 ± 20	58 ± 14	47 ± 13	48 ± 12	-0.5 ± 1.0	L100346–
	56361.452	0.363–0.467	7 ± 16	3 ± 11	6 ± 12	3 ± 12		L100353
2013 March 24	56375.392	0.174–0.278	168 ± 51	131 ± 33	122 ± 32	103 ± 30	-1.2 ± 1.0	L107837–
	56375.413	0.294–0.399	1 ± 21	8 ± 18	13 ± 21	-70 ± 51		L107844
2013 April 22	56404.314	0.837–0.941	202 ± 42	123 ± 38	108 ± 34	104 ± 30	-1.8 ± 0.9	L124005–
	56404.335	0.958–0.062	208 ± 69	176 ± 43	119 ± 43	91 ± 45	-2.1 ± 1.4	L124012
2013 May 20	56432.238	0.715–0.820	171 ± 37	116 ± 40	93 ± 35	99 ± 31	-1.5 ± 0.9	L133624–
	56432.258	0.836–0.940	256 ± 75	161 ± 35	141 ± 37	73 ± 47	-2.8 ± 1.4	L133643[a]
2013 July 14	56487.087	0.695–0.800	116 ± 36	68 ± 36	38 ± 32	39 ± 32		L160506–
	56487.108	0.816–0.921	183 ± 41	164 ± 57	82 ± 50	91 ± 47		L160513
2014 January 15	56672.578	0.984–0.089	228 ± 37	129 ± 22	132 ± 22	89 ± 16	-2.3 ± 0.6	L198919–
	56672.599	0.104–0.209	237 ± 39	148 ± 25	126 ± 23	86 ± 18	-2.6 ± 0.6	L198926

[a] The relevant IDs are L133624–L133625, L133630–L133631, L133637–L133638 and L133642–L133643.

Table 3. LOFAR low-band image-plane observations of PSR J2215+5135. The flux densities are the averages from the two beams used in this study (Table 1). Otherwise, see Table 2 for a description of the columns.

Date	MJD	ϕ (range)	$S_{54\,\mathrm{MHz}}$ (mJy)	$S_{60\,\mathrm{MHz}}$ (mJy)	ID
2013	56515.995	0.294–0.373	-120 ± 170	40 ± 140	L167732
August 11/12	56516.008	0.373–0.452	-30 ± 180	530 ± 220	
	56516.022	0.452–0.532	-290 ± 170	-320 ± 200	
2013	56594.778	0.009–0.088	1570 ± 510	1980 ± 680	L183339
October 29	56594.792	0.088–0.167	2980 ± 920	2090 ± 710	
	56594.806	0.167–0.246	2680 ± 830	1230 ± 560	
2014	56746.365	0.726–0.805	-190 ± 270	100 ± 180	L214818
March 30	56746.379	0.805–0.885	1980 ± 640	1650 ± 530	
	56746.392	0.885–0.964	2700 ± 840	1890 ± 590	

All flux densities have been corrected for the background level in the vicinity of the source, and the uncertainty in this process is included in the overall flux density uncertainty, along with the calibration uncertainty and the statistical fitting error (all terms added in quadrature). Biases arising from the different techniques used are an additional, but second-order effect. Note that noise fluctuations and/or uncertainties in the background level can occasionally result in negative flux densities for the forced fits; however, all such cases in this paper are consistent with a zero-level flux density within 1.7σ at most.

On 2013 March 24, there were significant differences between the high-band flux densities in the two pointings (spaced by 30 min). Similar behaviour was seen on 2014 March 30 in the low band. The modulation index, $\sigma_S/\overline{S}$, where σ_S is the standard deviation of the flux densities and $\overline{S}$ is the mean flux density, ranges from about 0.7–1.1 for the full set of observations at each of the six different frequencies.

In Table 2, we have also calculated the in-band spectral index for each HBA run where there were at least three detections $> 3\sigma$ (relative to the local rms noise level, and not including the additional uncertainties discussed above). Typically, the source has a very steep spectrum between 124 and 185 MHz, although the uncertainties for the individual measurements are often significant. The median spectral index is $\sim\!-2$.

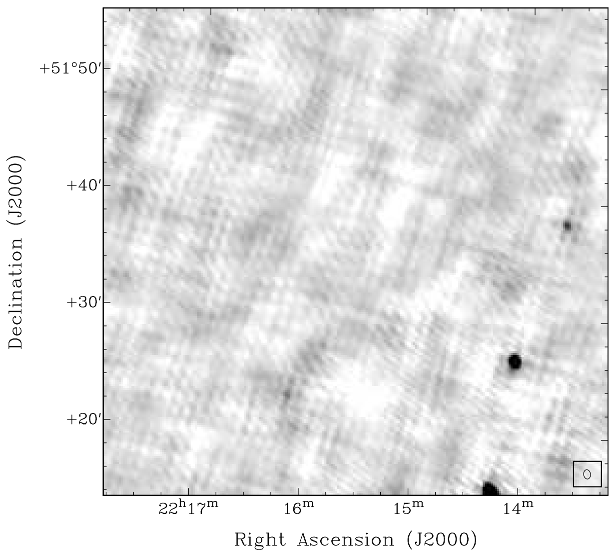

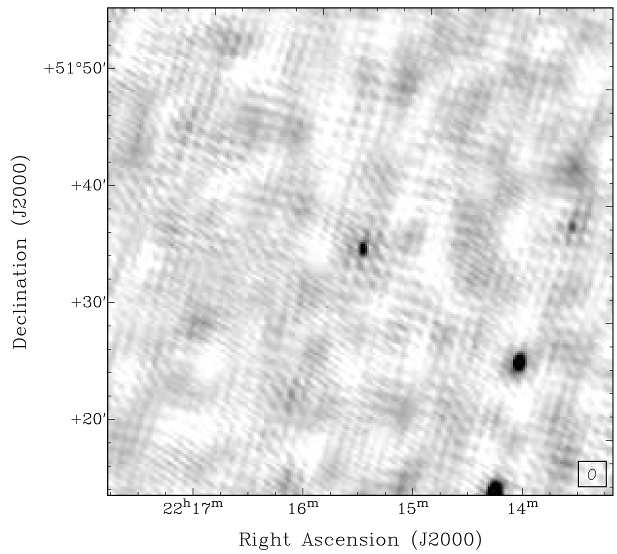

Figure 1. *Left*: 124-MHz LOFAR map from 2013 February 10 (MJD 56333.509), zoomed in on the position of PSR J2215+5135. The angular resolution is 48 arcsec × 35 arcsec (synthesized beam position angle 10°), and the rms noise level is 13 mJy beam^{-1}. The pulsar is not detected. *Right*: The same field, but from the observation on 2014 January 15 (MJD 56672.578). In this case, the angular resolution is 55 arcsec × 37 arcsec (beam position angle −11°), and the rms noise level is 15 mJy beam^{-1}. PSR J2215+5135 is now detected at approximately 15 times the local rms noise level, with a flux density of 228 mJy. The synthesized beam is shown in the bottom right-hand corner of each panel.

4 DISCUSSION

4.1 Evidence for eclipses

We now show that a pulsar origin is consistent with the source properties obtained from the LOFAR image-plane data. Firstly, the orbital phase, ϕ, of PSR J2215+5135 can be determined using the equation

$$\phi = \left[\frac{(t_{\rm obs} - T_{\rm asc}) \bmod P_{\rm orb}}{P_{\rm orb}} + 0.25\right] \bmod 1. \tag{1}$$

In Equation 1, $t_{\rm obs}$ is the Modified Julian Date (MJD) of the observation, with an additional barycentric correction; we used the software tools from Eastman, Siverd & Gaudi (2010) for this task. The orbital period $P_{\rm orb} = 0.172502104907(8)$ d, where the number in parentheses indicates the uncertainty on the least significant digit, and the time of the ascending node $T_{\rm asc} = 55186.164486(1)$ (Abdo et al. 2013; Hessels et al. in prep.). In our definition of orbital phase, the superior conjunction of the pulsar occurs at $\phi = 0.5$.

We calculated ϕ for each observation using Equation 1; these values are given in Tables 2 and 3. Although the individual data points sample $\sim$10 per cent of the orbit only, our combined HBA and LBA data sets provide good coverage across the full range of orbital phases.

Figure 2 shows flux density versus orbital phase for each of the six different frequencies. In each case, the observed change in the flux density implies that the variability is due to the eclipses of PSR J2215+5135.

4.2 Modelling the eclipses

We quantified the eclipse properties by using a Markov Chain Monte Carlo (MCMC) approach, fitting a double Fermi-Dirac-like function of the form

$$S(\phi) = S_0\left[\frac{1}{e^{(\phi-\mu_1)/\beta_1}+1} + \frac{1}{e^{-(\phi-\mu_2)/\beta_2}+1}\right] + S_{\rm b}, \tag{2}$$

to each light curve in Figure 2. In Equation 2, $S(\phi)$ is the flux density at orbital phase ϕ, S_0 is the uneclipsed, pulsed flux density, and $S_{\rm b}$ is the unpulsed, 'baseline' flux density. The parameters μ_1 and μ_2 are the orbital phases at which the pulsed flux density is half of its maximum value (i.e. $S_0/2$) during eclipse ingress and egress, respectively. Moreover, the constants β_1 and β_2 describe the slopes of ingress and egress, respectively; a smaller value corresponds to a more rapid, sharper transition.

We also accounted for the smearing of the eclipse profile due the integration time per data point being $\sim$10 per cent of the orbit. To do so, for each realisation of the eclipse light curve, we generated a high-resolution model containing 500 samples across an orbit. We then convolved it with a boxcar kernel having a width equal to the integration time, and using cyclic boundaries in order to ensure continuity and smoothness. For very small values of β_1 and/or β_2, this results in a sharp eclipse becoming 'ramp-like' (recall that the convolution of a Heaviside step function with a boxcar produces such a functional shape). For larger values of β_1 and/or β_2, both the underlying and smeared eclipse profiles are smoother.

Several possible variants of Equation 2 were trialled, with the number of free parameters adjusted. To distinguish between the different possibilities, we used the Akaike Information Criterion (e.g. Akaike 1974; Cavanaugh 1997; Burnham & Anderson 2004). We found that the data quality is not sufficient for increasingly sophisticated models. Hence, we used a simple model in which (i) there is no unpulsed component; (ii) the eclipses are symmetrical in time about the superior conjunction of the pulsar; and (iii) eclipse ingress and egress have symmetrical slopes. Equation 2 can therefore be rewritten as

$$S(\phi) = S_0\left[\frac{1}{e^{(\phi-\mu)/\beta}+1} + \frac{1}{e^{-(\phi-(1-\mu))/\beta}+1}\right], \tag{3}$$

where we have defined $\beta_1 = \beta_2 \equiv \beta$, and $1 - \mu_2 = \mu_1 \equiv \mu$.

The model fits are overplotted on the light curves in Figure 2. Each fit was generated using the set of parameters with the maximum posterior probability value; we list these in Table 4. We also

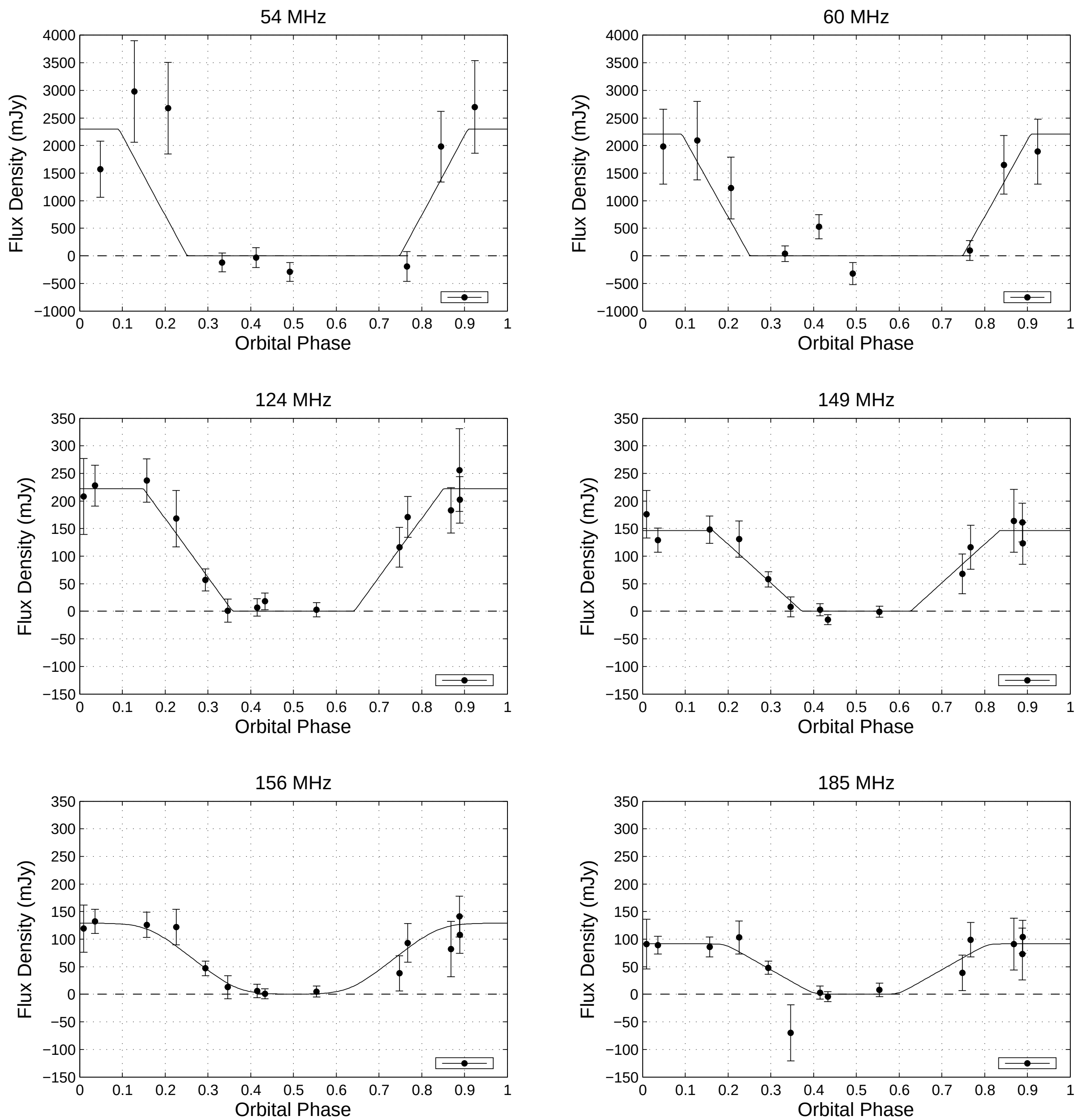

Figure 2. Flux density as a function of orbital phase (as defined in Equation 1, with the pulsar superior conjunction at $\phi = 0.5$) for the six frequencies used in this study. The average orbital phase is plotted for each separate observation; in the bottom right-hand corner of each plot, we indicate the phase range per data point. For the HBA data sets, the integration time on-source per data point is 22 min, although note that a 26-min scan duration is used for calculating the phase range, given that there is a calibrator observation between the two, 11-min snapshots (see Section 2.1 for further details). For the LBA panels, the integration time per data point is 20 min. In each panel, the solid line is a fitted double Fermi-Dirac-like function using the set of parameters for which the posterior probability was maximized (Section 4.2 and Table 4). Each model profile also takes into account that the eclipse is smeared out due to the limited sampling; this means that a very sharp eclipse becomes 'ramp-like', a shape that is seen in the majority of the profiles. On the other hand, smoother underlying profiles (e.g. at 156 MHz) are smoothed further by this effect; see Section 4.2 for futher details. All flux density error bars are $\pm 1\sigma$, while the dashed line indicates a zero-level flux density.

report the medians and means of the parameter distributions in Table 4; note that the distributions are sometimes skewed and the parameters correlated with each other. In particular, β is right skewed. For simplicity, and given the limitations of our analysis, we will use the mean values for S_0, μ and β in the rest of this paper; our conclusions are not affected significantly by this choice.

The β values in Table 4 are generally very small. Therefore, as explained above, the models for the majority of the light curves are not smooth. Moreover, all the β measurements are consistent with zero within the formal 95 per cent confidence interval, a value that would imply a perfectly sharp eclipse. Finer sampling is needed to quantify the eclipse sharpness more accurately.

4.3 Eclipse properties

In Figure 2, the model light curves are eclipsed for longer at LBA frequencies. The frequency dependence is quantified in Figure 3, where we have plotted the eclipse FWHM, $1 - 2\mu$, as a function

Table 4. Properties of the parameter distributions used in the fitting of the light curves in Figure 2. For each parameter and frequency, we first list the value from the set that yielded the maximum posterior probability (MPP). This is followed by the median and mean, including the formal 1σ uncertainty for the latter.

Frequency	S_0 (mJy)			μ			β		
(MHz)	MPP	Median	Mean	MPP	Median	Mean	MPP	Median	Mean
54	2300	2380	2600 ± 990	0.172	0.165	0.152 ± 0.044	6.6×10^{-4}	0.019	0.025 ± 0.020
60	2210	2870	3410 ± 1640	0.172	0.127	0.114 ± 0.057	9.2×10^{-5}	0.041	0.042 ± 0.026
124	223	234	240 ± 40	0.254	0.244	0.240 ± 0.027	3.4×10^{-4}	0.024	0.027 ± 0.019
149	147	149	149 ± 14	0.269	0.266	0.266 ± 0.018	4.4×10^{-4}	0.014	0.016 ± 0.012
156	129	135	141 ± 36	0.264	0.253	0.246 ± 0.042	0.027	0.035	0.037 ± 0.024
185	91	95	96 ± 15	0.297	0.286	0.283 ± 0.034	8.5×10^{-3}	0.023	0.027 ± 0.021

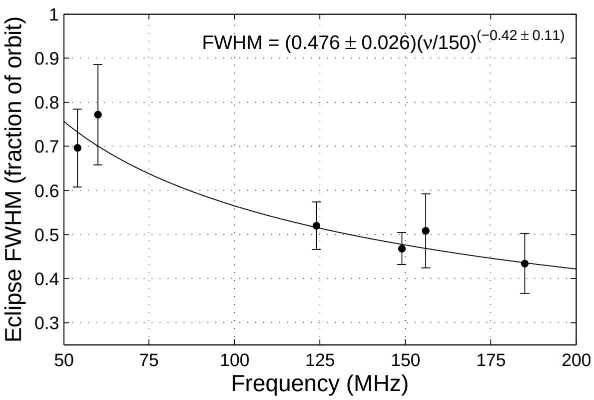

Figure 3. Eclipse FWHM, $1-2\mu$, as a function of frequency. The FWHMs are deduced from the mean μ values in Table 4. A power-law fit is also shown (reduced $\chi^2 = 0.22$).

of frequency. Fitting a power law to the data, the anti-correlation is found to have a frequency dependence of approximately $\nu^{-0.4}$: the source is eclipsed for ∼40–50 per cent of the orbit (∼1.7–2.1 h) in the high band, but ∼70–80 per cent (∼2.9–3.3 h) in the low band.

Other redback and black widow systems are known to be eclipsed for longer at lower frequencies (e.g. Archibald et al. 2009, 2013; Bhattacharyya et al. 2013). Various scenarios for an eclipsing mechanism are discussed, for example, in Thompson et al. (1994). Our image-plane observations suggest that the eclipses could be due to absorption, rather than scattering of the pulsations to a degree that greatly exceeds the pulse period, as the latter would still lead to image-plane detections. Indeed, Bhattacharyya et al. (2013) and Roy et al. (2015), the latter using simultaneous imaging and beamformed data, proposed that cyclotron-synchrotron absorption may be responsible for the eclipses of PSR J1544+4937 and PSR J1227−4853 / XSS J12270−4859.

In the case of PSR J2215+5135, observations that sample full individual orbits, with much finer orbital phase resolution, are needed to confirm the anti-correlation of eclipse length with frequency, which we regard as preliminary given the current evidence. This is particularly due to the relatively small number of data points, and also because the eclipses may be dynamic, with properties changing from orbit to orbit (e.g. Archibald et al. 2009, 2013; Bhattacharyya et al. 2013).

4.4 Radio spectrum

We plot the high-band spectral index as a function of orbital phase in the left panel of Figure 4. No statistically significant correlations are found, although there is a very tentative hint of spectral flattening during eclipse ingress, which would be consistent with the pulsar being eclipsed for longer at lower frequencies.

A LOFAR radio spectrum from 54–185 MHz, derived using the mean fitted flux densities from Table 4, is shown in the right panel of Figure 4. The spectral index is -2.82 ± 0.27. The predicted 74-MHz flux density is about 70 per cent higher than the recently-catalogued VLSS Redux (VLSSr; Lane et al. 2014) measurement, the latter being 670 ± 110 mJy when placed on the Baars et al. (1977) scale. However, the orbital phases covered by the VLSS suggest that the pulsar was partially eclipsed on average, potentially explaining the discrepancy.

5 CONCLUSIONS

Using interferometric observations in both the LOFAR high and low bands, we have detected the eclipses of the redback millisecond pulsar J2215+5135 in the image plane. By modelling the light curves at six different frequencies, we find preliminary evidence that the eclipse duration is longer at lower frequencies, with a frequency dependence of approximately $\nu^{-0.4}$.

The fact that the eclipses are observed in our imaging data suggests that the pulsed emission is being absorbed by the eclipsing screen(s), as scattering would still lead to image-plane detections of the pulsar when it is at superior conjunction. Whether PSR J2215+5135 shares a common eclipsing mechanism with other redbacks and black widows remains to be determined.

Current wide-field, low-frequency, image-plane searches for variables and transients (e.g. Bell et al. 2014; Obenberger et al. 2014; Stewart et al. 2016) have the potential to be able to uncover more redbacks and black widows, as well as other types of pulsars, particularly those that are very steep spectrum (such as PSR J2215+5135), highly polarized (e.g. Navarro et al. 1995), and/or highly scattered by the intervening interstellar medium along the line of sight (e.g. Dembska et al. 2015). Simultaneous image-plane and beamformed observations (e.g. Stappers et al. 2011; Roy et al. 2015) will be the most robust method for studying these systems in the radio domain.

ACKNOWLEDGEMENTS

We thank the referee for their comments and suggestions that significantly improved the presentation of this paper. We also thank the ASTRON Radio Observatory, particularly Michiel Brentjens and Carmen Toribio, for their considerable efforts in setting up the observations and pre-processing the raw data.

This project was supported by European Research Council

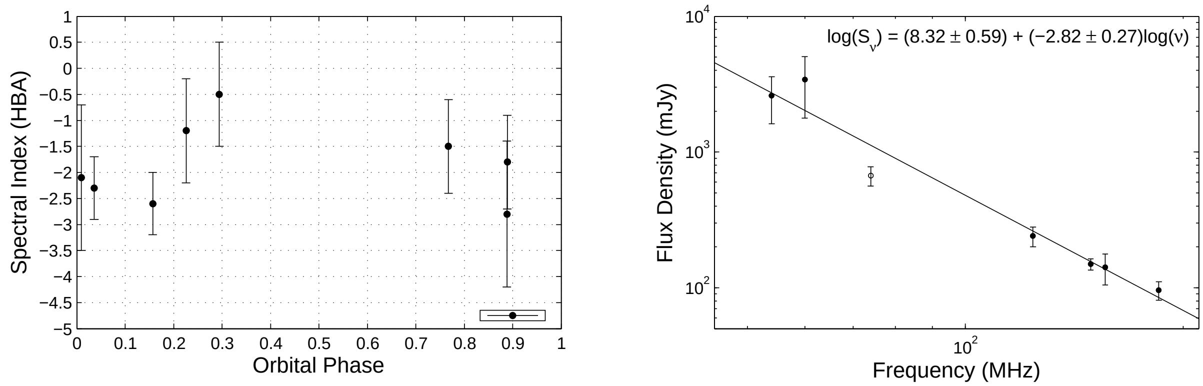

Figure 4. *Left*: Spectral index in the high band, as a function of orbital phase. We follow the same conventions as in Figure 2. *Right:* Radio spectrum for PSR J2215+5135. The filled circles are the LOFAR mean fitted flux densities from Table 4, and the open circle is the 74-MHz VLSSr flux density, adjusted to the scale of Baars et al. (1977). A linear least-squares fit in $\log(S_\nu)$–$\log(\nu)$ space, with inverse-variance weighting, to the six LOFAR data points, is shown (solid line); the reduced χ^2 value is 0.59.

Advanced Grant 267697 "4 Pi Sky: Extreme Astrophysics with Revolutionary Radio Telescopes", European Research Council Advanced Grant 247295 "AARTFAAC", and the European Union Seventh Framework Programme under grant agreement PIIF-GA-2012-332393. J.W.T.H. acknowledges funding from a NWO Vidi fellowship and European Research Council Starting Grant "DRAGNET" (337062). S.C. acknowledges financial support from the UnivEarthS Labex program of Sorbonne Paris Cité (ANR-10-LABX-0023 and ANR-11-IDEX-0005-02). L.H.A.S. acknowledges partial funding from the research programme of the Netherlands eScience Center (www.nlesc.nl). The financial assistance of the South African SKA Project (SKA SA) towards this research is hereby acknowledged. Opinions expressed and conclusions arrived at are those of the authors and are not necessarily to be attributed to the SKA SA.

LOFAR, the Low Frequency Array designed and constructed by ASTRON, has facilities in several countries, that are owned by various parties (each with their own funding sources), and that are collectively operated by the International LOFAR Telescope (ILT) foundation under a joint scientific policy.

The National Radio Astronomy Observatory is a facility of the National Science Foundation operated under cooperative agreement by Associated Universities, Inc.

REFERENCES

Abdo A. A. et al., 2013, ApJS, 208, 17
Akaike H., 1974, IEEE Trans. Autom. Contr., 19, 716
Antoniadis J. et al., 2013, Science, 340, 448
Archibald A. M. et al., 2009, Science, 324, 1411
Archibald A. M., Kaspi V. M., Hessels J. W. T., Stappers B., Janssen G., Lyne A., 2013, ApJ, submitted (arXiv:1311.5161)
Archibald A. M. et al., 2015, ApJ, 807, 62
Baars J. W. M., Genzel R., Pauliny-Toth I. I. K., Witzel A., 1977, A&A, 61, 99
Bassa C. G. et al., 2014, MNRAS, 441, 1825
Bell M. E. et al., 2014, MNRAS, 438, 352
Benvenuto O. G., De Vito M. A., Horvath J. E., 2014, ApJ, 786, L7
Bhattacharyya B. et al., 2013, ApJ, 773, L12
Breton R. P. et al., 2013, ApJ, 769, 108
Bridle A. H., Schwab F. R., 1999, in Taylor G. B., Carilli C. L., Perley R. A., eds, ASP Conf. Ser. Vol. 180, Synthesis Imaging in Radio Astronomy II, Astron. Soc. Pac., San Francisco, p. 371
Briggs D. S., 1995, PhD thesis, New Mexico Institute of Mining and Technology
Burgay M. et al., 2006, MNRAS, 368, 283
Burnham K. P., Anderson D. R., 2004, Sociological Methods & Research, 33, 261
Cavanaugh J. E., 1997, Statistics & Probability Letters, 33, 201
Chen H.-L., Chen X., Tauris T. M., Han Z., 2013, ApJ, 775, 27
Cohen A. S., Lane W. M., Cotton W. D., Kassim N. E., Lazio T. J. W., Perley R. A., Condon J. J., Erickson W. C., 2007, AJ, 134, 1245
Condon J. J., Cotton W. D., Greisen E. W., Yin Q. F., Perley R. A., Taylor G. B., Broderick J. J., 1998, AJ, 115, 1693
Crawford F. et al., 2013, ApJ, 776, 20
Dembska M., Basu R., Kijak J., Lewandowski W., 2015, MNRAS, 449, 1869
Demorest P. B., Pennucci T., Ransom S. M., Roberts M. S. E., Hessels J. W. T., 2010, Nature, 467, 1081
Eastman J., Siverd R., Gaudi B. S., 2010, PASP, 122, 935
Fender R., Wijers R., Stappers B., LOFAR Transients Key Science Project, 2008, arXiv:0805.4349
Fruchter A. S., Stinebring D. R., Taylor J. H., 1988, Nature, 333, 237
Hessels J. W. T. et al., 2011, in Burgay M., D'Amico N., Esposito P., Pellizzoni A., Possenti A., eds, AIP Conf. Proc. Vol. 1357, Radio Pulsars: An Astrophysical Key to Unlock the Secrets of the Universe, p. 40
Keith M. J. et al., 2011, MNRAS, 414, 1292
Kluzniak W., Ruderman M., Shaham J., Tavani M., 1988, Nature, 334, 225
Lane W. M., Cotton W. D., van Velzen S., Clarke T. E., Kassim N. E., Helmboldt J. F., Lazio T. J. W., Cohen A. S., 2014, MNRAS, 440, 327
Obenberger K. S. et al., 2014, ApJ, 788, L26
Offringa A. R., de Bruyn A. G., Biehl M., Zaroubi S., Bernardi G., Pandey V. N., 2010, MNRAS, 405, 155
Offringa A. R., van de Gronde J. J., Roerdink J. B. T. M., 2012a, A&A, 539, A95
Offringa A. R., de Bruyn A. G., Zaroubi S., 2012b, MNRAS, 422, 563

McKean J. et al., 2011, arXiv:1106.1041
Navarro J., de Bruyn A. G., Frail D. A., Kulkarni S. R., Lyne A. G., 1995, ApJ, 455, L55
Papitto A. et al., 2013, Nature, 501, 517
Patruno A. et al., 2014, ApJ, 781, L3
Ransom S. M. et al., 2011, ApJ, 727, L16
Ray P. S. et al., 2012, arXiv:1205.3089
Rengelink R. B., Tang Y., de Bruyn A. G., Miley G. K., Bremer M. N., Roettgering H. J. A., Bremer M. A. R., 1997, A&AS, 124, 259
Roberts M. S. E., 2013, in van Leeuwen J., ed., Proc. IAU Symp. 291, Neutron Stars and Pulsars: Challenges and Opportunities after 80 Years. Cambridge Univ. Press, Cambridge, p. 127
Romani R. W., Filippenko A. V., Silverman J. M., Cenko S. B., Greiner J., Rau A., Elliott J., Pletsch H. J., 2012, ApJ, 760, L36
Romani R. W., Graham M. L., Filippenko A. V., Kerr M., 2015, ApJ, 809, L10
Roy J. et al., 2015, ApJ, 800, L12
Sault R. J., Teuben P. J., Wright M. C. H., 1995, in Shaw R. A., Payne H. E., Hayes J. J. E., eds, ASP Conf. Ser. Vol. 77, Astronomical Data Analysis Software and Systems IV, Astron. Soc. Pac., San Francisco, p. 433
Scheers L. H. A., 2011, PhD thesis, Astronomical Institute Anton Pannekoek, Univ. Amsterdam
Schroeder J., Halpern J., 2014, ApJ, 793, 78
Spreeuw J. N., 2010, PhD thesis, Astronomical Institute Anton Pannekoek, Univ. Amsterdam
Stappers B. W. et al., 1996, ApJ, 465, L119
Stappers B. W. et al., 2011, A&A, 530, A80
Stappers B. W. et al., 2014, ApJ, 790, 39
Stewart A. J. et al., 2016, MNRAS, 456, 2321
Strader J. et al., 2015, ApJ, 804, L12
Swinbank J. D. et al., 2015, A&C, 11, 25
Tasse C., van der Tol S., van Zwieten J., van Diepen G., Bhatnagar S., 2013, A&A, 553, A105
Thompson C., Blandford R. D., Evans C. R., Phinney E. S., 1994, ApJ, 422, 304
van den Heuvel E. P. J., van Paradijs J., 1988, Nature, 334, 227
van der Tol S., Jeffs B. D., van der Veen A.-J., 2007, IEEE Trans. Sig. Proc., 55, 4497
van Haarlem M. P. et al., 2013, A&A, 556, A2

This paper has been typeset from a TEX/ LATEX file prepared by the author.